XL CILAMCE
IBERO-LATIN AMERICAN CONGRESS ON COMPUTATIONAL METHODS IN ENGINEERING
NOVEMBER 11-14, 2019
Praiamar Natal Hotel & Convention Natal, RN-BRAZIL

A COMPARISON BETWEEN SMOOTHED PARTICLE HYDRODYNAMICS (SPH) AND MOVING PARTICLE SEMI-IMPLICIT (MPS) METHODS FOR DAM-BREAKING EVENT

Rubens A. Amaro Jr
Liang-Yee Cheng
rubens.amaro@usp.br
cheng.yee@usp.br
Department of Construction Engineering, University of São Paulo
Av. Prof. Almeida Prado, trav. 2, 83 - Cidade Universitária, 05508-900, São Paulo, SP, Brazil
Sergei K. Buruchenko
buruchenkosk@susu.ru
Snezhinsk, Russian Federation

Abstract. Lagrangian particle-based methods have opened new perspectives for the investigation of complex problems with large free-surface deformation. Some well-known particle-based methods adopted to solve non-linear hydrodynamics problems are the smoothed particle hydrodynamics (SPH) and moving particle semi-implicit (MPS). Both methods modeled the continuum by a system of Lagrangian particles (points) but adopting distinct approaches for the numerical operators, pressure calculation, and boundary conditions. Despite the ability of the particle-based methods in modeling highly nonlinear hydrodynamics, some shortcomings, such as unstable pressure computation and high computational cost still remains. In order to assess the performance of these two methods, the weakly-compressible SPH parallel solver, DualSPHysics, and an in-house incompressible MPS solver are adopted in this work. Two test cases consisting of 3D dam-breaking problems are simulated and wave heights, pressures and forces are compared with available experimental data. The influence of the artificial viscosity on the accuracy of SPH is investigated. Computational times of both solvers are also compared. Finally, the relative benefits of the methods for solving free-surface problems are discussed, therefore providing directions of their applicability.

Keywords: Dam-break, SPH, MPS, Particle method, Artificial viscosity

1 Introduction

Particle-based methods are very effective for the simulation of hydrodynamics problems involving free surface, fragmentation and merging, large deformation, complex-shaped bodies and moving boundaries. Among those methods, smoothed particle hydrodynamics (SPH) and moving particle semi-implicit (MPS) have opened new perspectives to solve non-linear hydrodynamics problems. The SPH was first introduced in astrophysics by Gingold and Monaghan [1] and Lucy [2], whereas the MPS was proposed by Koshizuka et al. [3] for the simulation of incompressible free-surface flow. Both methods solve the governing equations of continuum by replacing the differential operators with discrete operators derived from a particle interaction model based on a kernel or weight function. Besides the difference between the discrete operators adopted by these methods, weakly-compressible SPH uses an explicit algorithm and an equation of state assuming a limited-compressible flow, while MPS is based on semi-implicit algorithm with the solution of the pressure Poisson equation (PPE) to model the incompressible flow.

Despite the ability of the particle-based methods in modeling highly distorted free-surface flow, wave breaking and flow separation and coalescence, some shortcomings of these methods, such as unstable pressure computation and high computational cost still remains. Different approaches were proposed to achieve more stable computation [4], as well as parallel processing in central processing units (CPUs) [5] or graphics processing units (GPUs) [6] were performed to solve large-scale practical engineering problems in a reasonable processing time.

In order to identify the performance of each formulation under specific applications, several works compared weakly-compressible and fully-incompressible particle-based methods. Lee et al. [7] presented comparisons between the classical weakly-compressible SPH and the incompressible SPH (ISPH) [8] methods. According their work, the ISPH yielded much more reliable results than SPH, shown smoother velocity and pressure fields. Hughes and Graham [9] also compared SPH and ISPH for dam-breaking problems and regular water waves impacting against a vertical wall. Moving least-squares (MLS) or Shephard filtering density renormalization methods and specific boundary condition formulations were used. As a result, they concluded that in the optimum configuration, SPH performs at least as well as ISPH, and in some respects clearly performs better. In Hashimoto et al. [10], comparisons of experiment data and the SPH and MPS results were performed on forced roll tests of a two-dimensional damaged car ferry. Both numerical results are in good agreement with the model experiment when the entrapped air effect is relatively small. However, the agreement become worse when air entrapped occurs. Based on the experimental results for a collapsing water column with a rigid obstacle and on wet bed, Abdelrazek et al. [11] compared the numerical results obtained by SPH and standard MPS, i.e., without recent improvements. As a result, more stable particles distributions were obtained by SPH due its artificial viscosity, along with smoother predicted free surface and pressure time series. Despite the better performance of the SPH, the authors highlighted the independence of MPS regarding the parameters used in SPH, which usually require appropriate tuning. In Bakti et al. [12], experiments of two-dimensional dam-breaking and harmonically oscillated sloshing tank were adopted as references to compare the results obtained by SPH and MPS. A free-decay test case also was studied. In the dam-breaking case, a new relation between the artificial viscosity coefficient of the SPH and the kinematic viscosity of the MPS was obtained. Both methods showed reasonably good agreement with the experimental results. However, a small gap between the fluid and the wall was shown in the SPH simulation due to the formulation of the impenetrable wall boundary condition. The authors also pointed out that the use of SPH, without a careful treatment, can significantly overestimate the impact pressure. Moreover, SPH seems to be more efficient computationally but without solving PPE is generally less accurate.

From the previous studies, it is clear that the strong or weak points of each method depend on the phenomena being investigated, the required output, the available computational resources and the improved variants adopted. The aim of this paper is to explore the merits of SPH and MPS in simulations of free-surface flow problems, therefore providing additional results for the discussions

towards the applicability of both methods. Here, the open source DualSPHysics [13] based on the weakly-compressible SPH and an in-house program based on MPS were adopted for the simulations. Two test variants of 3D dam-breaking problems [14,15] were considered and the computed wave heights, pressures and forces were compared with available experimental data. The computational times for each method are also presented.

2 Governing equations and methods

In this section, the numerical methods are described briefly.

2.1 Governing equations

The governing equations of incompressible flow of viscous Newtonian fluids are expressed by the conservation laws of mass and momentum:

$$\frac{D\rho}{Dt} = \rho\nabla\cdot\mathbf{u} = 0, \tag{1}$$

$$\frac{D\mathbf{u}}{Dt} = -\frac{\nabla P}{\rho} + \nu\nabla^2\mathbf{u} + \mathbf{f}, \tag{2}$$

where ρ is the fluid density, $\mathbf{u}$ is the velocity vector, P is the pressure, ν is the kinematic viscosity and $\mathbf{f}$ is the external body force per unit mass vector.

2.2 Smoothed particle hydrodynamics (SPH)

SPH is defined as a method for obtaining approximate numerical solutions of fluid dynamics equations by replacing the fluid with a set of particles. The physical properties, for example the time derivatives of mass and velocity on each point are obtained summing weighted contributions from the surrounding points. These points (particles) then move with the fluid. The method uses discrete approximations for interpolation integrals to transform differential equations of fluid dynamics into particle summations. For this purpose, special weighting functions called smoothing kernels are employed. A complete review on standard SPH can be found at Monaghan [16]. The artificial viscosity scheme, proposed by Monaghan [17], is adopted here:

$$\frac{d\mathbf{u}_a}{dt} = -\sum_b m_b\left(\frac{P_b+P_a}{\rho_b\rho_a} + \Pi_{ab}\right)\nabla_a W_{ab} + \mathbf{g}, \tag{3}$$

where m, P and ρ are the mass, pressure and density that correspond to particles a or b, and $\mathbf{g}$ is the gravity acceleration vector. The viscosity term Π_{ab} is given by:

$$\Pi_{ab} = \begin{cases} -\frac{\alpha\overline{c_{ab}}\mu_{ab}}{\overline{\rho_{ab}}} & \mathbf{v}_{ab}\cdot\mathbf{r}_{ab} < 0 \\ 0 & \mathbf{v}_{ab}\cdot\mathbf{r}_{ab} > 0 \end{cases}, \tag{4}$$

where $\mathbf{r}_{ab} = \mathbf{r}_a - \mathbf{r}_b$ and $\mathbf{v}_{ab} = \mathbf{v}_a - \mathbf{v}_b$, with $\mathbf{r}_k$ and $\mathbf{v}_k$ being the particle position and velocity respectively. $\mu_{ab} = h\mathbf{v}_{ab}\cdot\mathbf{r}_{ab}/(\mathbf{r}_{ab}^2+\eta^2)$, $\overline{c_{ab}} = 0.5(c_a+c_b)$ states the mean speed of sound evaluated at a or b, $\bar{\rho}_{ab} = 0.5(\rho_a+\rho_b)$ represents the mean density, $\eta^2 = 0.01h^2$ and α is the artificial viscosity that needs to be tuned in order to introduce the proper dissipation. The smoothing length h controls the size of the area around one particle in which neighboring particles are considered.

Symbol W_{ab} indicates the SPH kernel function, which is used here to "weight" the particle interactions. The kernel is expressed as a function of the non-dimensional distance between particles $q = |\mathbf{r}_{ab}|/h$, and can be obtained by the Wendland function [18]:

$$W_{ab} = \alpha_D\left(1-\frac{q}{2}\right)^4(2q+1) \quad 0\le q\le 2\,, \tag{5}$$

where $\alpha_D = 7/4\pi h^2$ in 2D and $\alpha_D = 21/16\pi h^3$ in 3D.

The delta-SPH variant [19], which introduces a proper artificial diffusive term, is applied to the continuity equation, see Eq. (1), in order to suppress the spurious numerical high-frequency oscillations that generally affect the pressure field of the weakly-compressible SPH schemes. The delta-SPH discretizes the continuity equation as

$$\frac{d\rho_a}{dt} = \sum_b m_b \mathbf{v}_{ab} \cdot \nabla_a W_{ab} + 2\delta h c_0 \sum_b (\rho_b - \rho_a) \frac{\mathbf{r}_{ab} \cdot \nabla_a W_{ab}}{\mathbf{r}_{ab}^2} \frac{m_b}{\rho_b}, \tag{6}$$

In this work, $\delta = 0.1$ was adopted for all simulations.

Following the work of Monaghan [20], the fluid is considered as weakly-compressible and an equation of state is used to determine fluid pressure based on particle density. The Tait equation of state is commonly used:

$$p = \frac{\rho_0 {c_0}^2}{\gamma} \left[\left(\frac{\rho}{\rho_0} \right)^{\gamma} - 1 \right], \tag{7}$$

In the above equation, $\gamma = 7$, ρ_0 is the reference density and c_0 is an artificial speed of sound. The artificial speed of sound is adopted instead of the real speed one because the later require a very small time step. In order to keep density variations less than 1%, the value of c_0 is chosen about ten times the maximum velocity $|\mathbf{v}_{max}|$, according to Monaghan [20].

The dynamic boundary conditions described in Crespo et al. [21] are used in this work. The boundary particles satisfy the same continuity equation as the fluid particles, therefore, their density and pressure are also computed. Hence, when a fluid particle approaches the boundary particles, and get inside the kernel range of the boundary particles, the density of the later increases. As a result, the force exerted on the fluid particle increases due to the pressure term in the momentum equation creating a repulsive mechanism between fluid and boundary.

More detailed descriptions regarding the characteristics of the open source DualSPHysics can be found in Crespo et al. [13].

2.3 Moving particle semi-implicit (MPS)

In the MPS method, the differential operators of the governing equations of continuum are replaced by discrete operators derived based on a weight function ω_{ij}, which accounts the influence of a particle j in the neighborhood of the particle i, and is given by:

$$\omega_{ij} = \begin{cases} \frac{r_e}{|\mathbf{r}_{ij}|} - 1 & |\mathbf{r}_{ij}| \leq r_e \\ 0 & |\mathbf{r}_{ij}| > r_e \end{cases}, \tag{8}$$

where r_e is the effective radius that limits the range of influence and $|\mathbf{r}_{ij}| = |\mathbf{r}_j - \mathbf{r}_i|$ is the distance between i and j.

The summation of the weight of all the particles in the neighborhood of the particle i is defined as its particle number density n_i, which is proportional to the fluid density:

$$n_i = \sum_{j \neq i} \omega_{ij}, \tag{9}$$

For a scalar function ϕ, the gradient and Laplacian operators are, respectively, defined as:

$$\langle \nabla \phi \rangle_i = \frac{d}{n^0} \sum_{j \neq i} \frac{\phi_j - \phi_i}{|\mathbf{r}_{ij}|^2} \mathbf{r}_{ij} \omega_{ij}, \tag{10}$$

$$\langle \nabla^2 \phi \rangle_i = \frac{2d}{\lambda_i n^0} \sum_{j \neq i} (\phi_j - \phi_i) \omega_{ij}, \tag{11}$$

where d is the number of spatial dimensions and n^0 is the particle number density for a fully filled compact support. Finally, λ_i is a correction parameter so that the variance increase is equal to that of the analytical solution, and is calculated by:

$$\lambda_i = \frac{\sum_{j \neq i} \omega_{ij} |\mathbf{r}_{ij}|^2}{\sum_{j \neq i} \omega_{ij}}, \tag{12}$$

To solve the incompressible viscous flow, a semi-implicit algorithm is used in the MPS method.

At first, predictions of the particle's velocity ($\mathbf{u}_i^*$) and position ($\mathbf{r}_i^*$) are carried out explicitly by using viscosity and external forces terms of the momentum conservation, see Eq. (2). Then the pressure of all particles is calculated by the PPE as follows:

$$\langle \nabla^2 P \rangle_i^{t+\Delta t} - \frac{\rho}{\Delta t^2} \alpha_c P_i^{t+\Delta t} = -\gamma \frac{\rho}{\Delta t^2} \frac{n_i^* - n^0}{n^0}, \tag{13}$$

where Δt is the time step, n_i^* is the particle number density calculated based on the displacement of particles obtained in the prediction step, α_c is the coefficient of artificial compressibility and γ is the relaxation coefficient. Both α_c and γ are used to improve the stability of the computation method. In order to prevent instability issues induced by attractive pressure and reduces the effect of nonuniform particle distribution, we adopted the first order pressure gradient [22]:

$$\langle \nabla P \rangle_i = \left[\sum_{j \neq i} \omega_{ij} \frac{\mathbf{r}_{ij}}{|\mathbf{r}_{ij}|} \otimes \frac{\mathbf{r}_{ij}^T}{|\mathbf{r}_{ij}|} \right]^{-1} \sum_{j \neq i} \frac{P_j - \hat{P}_i}{|\mathbf{r}_{ij}|^2} \mathbf{r}_{ij} \omega_{ij}, \tag{14}$$

where $\hat{P}_i$ is the minimum pressure between the neighborhood of the particle i.

Finally, the velocity of the particles is updated by:

$$\mathbf{u}_i^{t+\Delta t} = \mathbf{u}_i^* - \frac{\Delta t}{\rho} \langle \nabla P \rangle_i^{t+\Delta t}, \tag{15}$$

and the new positions of the particles are corrected by:

$$\mathbf{r}_i^{t+\Delta t} = \mathbf{r}_i^* + \left(\mathbf{u}_i^{t+\Delta t} - \mathbf{u}_i^* \right) \Delta t. \tag{16}$$

Solid wall is modeled by using three layers of fixed particles. The particles that form the layer in contact with the fluid are denominated wall particles, of which the pressure is computed by solving the PPE, see Eq. (8), together with the fluid particles. The particles that form two other layers are denominated dummy particles, which are used to ensure the correct calculation of the particle number density of the wall particles. Pressure is not calculated in the dummy particles. As boundary condition of rigid walls, the no-slip condition is considered on the wall. The Dirichlet pressure boundary condition is imposed to the particles identified as free surface and it is considered during the implicit step of the method. In the present work, the neighborhood particles centroid deviation (NPCD) method [23] is adopted. By accurately identifying free-surface particles, the NPCD method improves the stability and accuracy of the pressure computation, by eliminating spurious oscillations due to misdetection of free-surface particles inside the fluid domain. It provides satisfactory results even by using only the particle number density deviation as the source term in Eq. (13).

3 Results

Two dam-breaking cases are studied. First, computed wave heights and pressures are compared to experimental [14] and numerical ones [24]. After that, computed and experimental [15] forces on a box are compared for a second dam-breaking case.

For all simulations, we adopted the density of the fluid as ρ = 1000 kg/m^3, and the gravity acceleration g = 9.81 m/s^2. The artificial speed of sound $c_0 = 20\sqrt{gH_w}$, where H_w is the initial water column height, was used in SPH. The coefficients $\alpha_c = 10^{-8}$ ms^2/kg and $\gamma = 0.01$ were adopted for the MPS. Concerning the time step, we set CFL = 0.2 for both methods.

3.1 3D dam-breaking flow – Wave height and pressure

The first case (Case 1) is based on the experiment performed by Kleefsman et al. [14]. The initial geometry, main dimensions, wave probes positions (H_1, H_2, H_3 and H_4) and pressure sensors (P_1, P_2 and P_3) on the box are shown in Fig. 1.

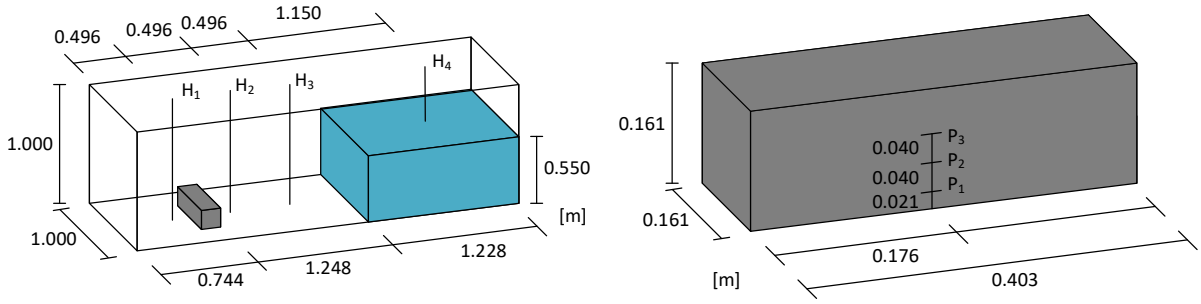

Figure 1. Initial geometry, main dimensions, wave probes (H_1, H_2, H_3 and H_4) (left) and pressure sensors (P_1, P_2 and P_3) on the box (right) [14]

Similar to the investigation performed for a 2D dam-breaking flow in Bakti et al. [12], four different artificial viscosity values were adopted here for the 3D simulations with SPH, and their effects on the free-surface flow and pressure on the box are discussed. The artificial viscosity is generally adopted to smooth the unphysical numerical oscillations, although it can also introduce undesirable numerical problems, e.g., excess dissipation and false shearing torque in rotating flows [25]. According to Monaghan [16], the continuum limit of the viscosity shows that, for the Wendland kernel (Eq. (5)) the kinematic (ν) and artificial (α) viscosities in three dimensions can be related by $\nu_a = \alpha_a h c_a/10$. Assuming the artificial speed of sound almost constant c_0, as done in Bakti et al. [12], the relation $\nu_0 = \alpha_0 h c_0/10$ was used here to correlate kinematic viscosity and the artificial viscosity adopted in SPH. Numerical parameters and processing times are presented in Table 1.

Table 1. Numerical parameters and processing time of Case 1

Parameter	SPH	MPS
Viscosity (ν_0)	5.2x10^{-3}, 5.2x10^{-4}, 5.2x10^{-5}, 5.2x10^{-6} m²/s	10^{-6} m²/s
Artificial viscosity (α_0)	0.1, 0.01, 0.001, 0.0001	-
Particle distance (l_0)	0.0075 m	0.0075 m
Radius of support	$2h = 3l_0$	$r_e = 2.1l_0$
Fluid particles	1.6x10^6	1.6x10^6
Boundary particles	2.1x10^5	6.5x10^5
Simulation time	6 s	6 s
Time step (Δt)	3.8x10^{-5} s*	3x10^{-4} s
Computational time	0d4h00m$^\blacklozenge$	2d14h00m†

* Based on the number of computational steps. DualSPHysics uses a variable time steps restrict by CFL and the diffusion stability criteria [13].
♦ GPU Nvidia Tesla K40m, 15 Multiprocessors (2880 cores), clock rate of 0.75 GHz and 11.519 GB of global memory.
† CPU Intel® Xeon® Processor E5 v2 Family, processor base frequency of 2.80 GHz, 20 cores and 126 GB of memory.

The snapshots of the free-surface deformation computed by the SPH ($\alpha_0 = 0.0001$) and MPS are illustrated in Fig. 2. Only free-surface particles are shown in the simulations. The colors on the free surface of the fluid particles are related to its dimensionless velocity magnitude $|\mathbf{v}|/\sqrt{2gH_w}$, where $H_w = 0.55$ m is the initial water column height. After hitting the weather side of the box, large splash is formed at the instant *t = 0.50 s*, and part of the wave wraps the box. The wave collides the corners of the tank wall, and the splash reaches the top of the domain at the instant *t = 0.75 s*, approximately. After that, at the instant *t = 1.05 s*, the reflected wave breaks and splashed fluid fall down due the gravity, followed by their merging near the box at the instant *t = 1.50 s*, approximately. Overall, both methods produce a similar fluid behavior, despite the lower spreading of the splash computed by the SPH at the instant *t = 1.05 s*. This difference might be attributed to the artificial viscosity in SPH, although a relatively low value was adopted here.

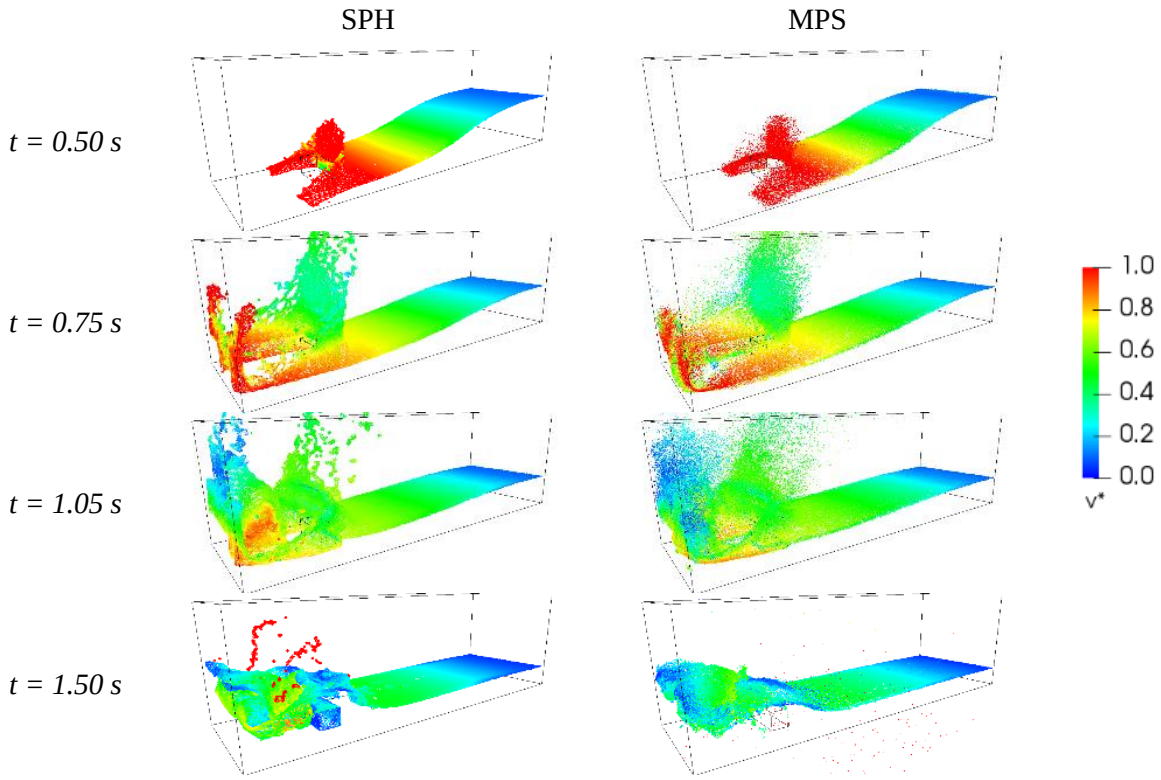

Figure 2. Snapshots of the dam-breaking simulations carried out with SPH adopting $\alpha_0 = 0.0001$ (left) and MPS (right)

Figure 3(a) shows the wave heights at the probe H_4. Compared to the experimental data, the water column collapsing occurs slightly slower for the SPH simulations with $\alpha_0 \leq 0.01$ and slightly faster for the MPS simulation. For the SPH simulation with $\alpha_0 = 0.1$, the delay is remarkable. All computed heights present a delay after the first reflected wave, at approximately $t = 2.7$ *s*. As reported in [26], these deviations might be related to the interaction with the boundary during the impact on the back and front walls, so that SPH might overestimate the boundary effect on the flow. On the other hand, these deviations occur in the MPS simulation due to an inherent numerical dissipation. In addition to the underestimated wave height computed by SPH during the second incoming wave, the numerical results are delayed in comparison with the experimental one, especially for SPH with $\alpha_0 = 0.1$, approximately at the instant $t = 4.5$ *s*.

Figure 3(b) illustrates the wave heights at the probe H_3. Until the instant $t = 2.0$ *s*, the computed wave heights are slightly higher than the experimental one. After that, the wave heights for both methods are in reasonable agreement with the experimental data. However, exceptions occur around the second wave impact, $t = 4.8$ *s*, where the SPH with $\alpha_0 \leq 0.01$ leads to higher waves and, as previous observed, there is a delay in relation to the experimental data.

The wave heights at the probe H_2 are provided in Fig. 3(c). The high values of the computed wave heights from $t = 0.75$ *s* to $t = 1.05$ *s* reflect the splashing fluid particles that reach the top of the domain. After the wave reflection, between the instants $t = 1.5$ *s* and $t = 2.5$ *s*, the wave heights computed by SPH with $\alpha_0 \leq 0.01$ are slighter higher than the experimentally measured one. As previous discussed for the probe H_3, the computed wave heights are in reasonable agreement with the experimental data, with exception of the instants after $t = 4.8$ *s*.

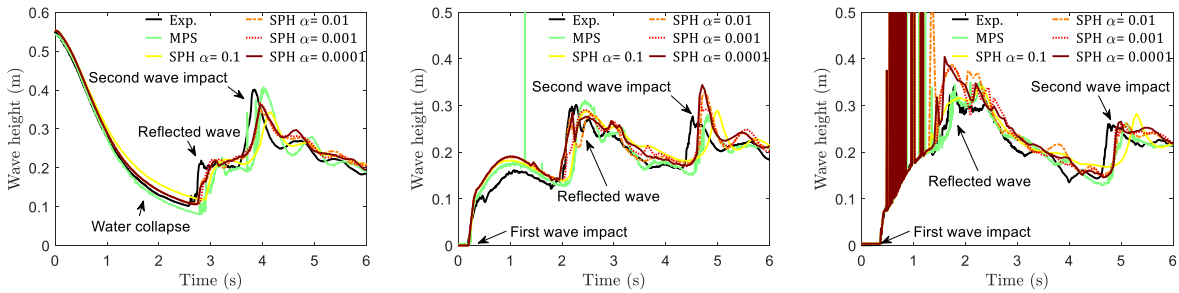

Figure 3. Wave height at probe (a) H_4, (b) H_3 and (c) H_2. Experimental data [14] and numerically computed using MPS and SPH

Overall, experimentally measured and numerically computed wave heights are in good agreements, except for SPH with the artificial viscosity $\alpha_0 \geq 0.1$, or $\nu_0 \geq O(10^{-2})$.

In Fig. 4, the computed pressure time series at P_1, P_2 and P_3, are compared with the experimental data [14]. In addition, numerical results by the mesh-based codes FreSCo [24] and ConFlow [14], both adopting volume of fluid (VOF) approach to handle free-surfaces, are shown. First of all, it is important to clarify how the computed pressure time series are obtained in each method. In MPS, the pressure calculated at the wall particle closer to the sensor position is considered. In SPH, the default output pressure of DualSPHysics is given by:

$$P_a = \frac{\sum_b P_b W_{ab}}{\sum_b W_{ab}}, \tag{16}$$

where P_b is the pressure of neighboring fluid particles b at the point a. Although Eq. (16) gives the spatial average pressure, instead the raw data at a specific point, it provides acceptable results for practical purposes.

The peak pressure at sensor P_1 is over predicted by MPS while is under predicted by SPH. On the other hand, computed peak pressure at sensor P_2 is in very well agreement with experimental data for MPS and SPH with $\alpha_0 = 0.0001$. For the sensor P_3, the peak pressure is well predicted by all SPH simulations but under predicted by MPS. One aspect to highlight here is that the computed impact pressure peak is highly sensitive to numerical parameters. The reason for this is out of the scope of the present work, but it is affected by discrete approximations, e.g., time step and spatial resolution, as well as numerical parameters, such as compressibility, relaxation coefficients, etc. In this way, discrepancies between experimentally measured and numerically computed peak pressures are expected.

After the first pressure peak, the pressures obtained by MPS are in good agreement with experiment ones. On the other hand, high-amplitude pressure oscillations are computed by SPH until *t = 1.5 s*. This might be related to the compression waves caused by the weakly-compressibility modeling of the SPH and will be investigate more carefully in the future. After the instant *t = 1.5 s*, the pressures computed by SPH with $\alpha_0 \leq 0.01$ are very similar, whereas the pressure oscillations computed by SPH with $\alpha_0 = 0.1$ increase after *t = 3.5 s*. In this way, $\alpha_0 \leq 0.01$, i.e., $\nu_0 \leq O(10^{-3})$, is preferable for this case.

As the peak values of hydrodynamic impact pressure show some randomness, an alternative reference for the comparison is the use of the impulse. This is because the momentum conservation should be satisfied, independent of the pressure peaks shape. Thus, for sake of simplicity, the pressure impulses I_p computed by SPH and MPS during the first 6 seconds were also compared with the experimental ones. The computed pressure impulses and their relative deviations, referred to the experimental ones, can be found in Table 2. The SPH underestimates the pressure impulses with a relative deviation around 29% for the sensor P_1. It ranges from 40% to 55% for the sensor P_2 and from 8% to 24% for the sensor P_3. The increase of the artificial viscosity leads to larger deviations, indicating that $\alpha_0 \leq 0.001$, i.e., $\nu_0 \leq O(10^{-4})$, is preferable to reproduce the hydrodynamic loads. On the other hand, MPS underestimates the pressure impulses with a relative deviation between 5% and

11%. Despite both numerical methods underestimate the experimental results, in terms of hydrodynamic loads, the pressures computed by MPS are more accurate than those obtained by SPH.

Concerning the processing time of each method, given in Table 1, the PPE system solver in MPS play a mandatory role in improving computational efficiency. It is evidenced by the much faster computation provided by the GPU-based calculations.

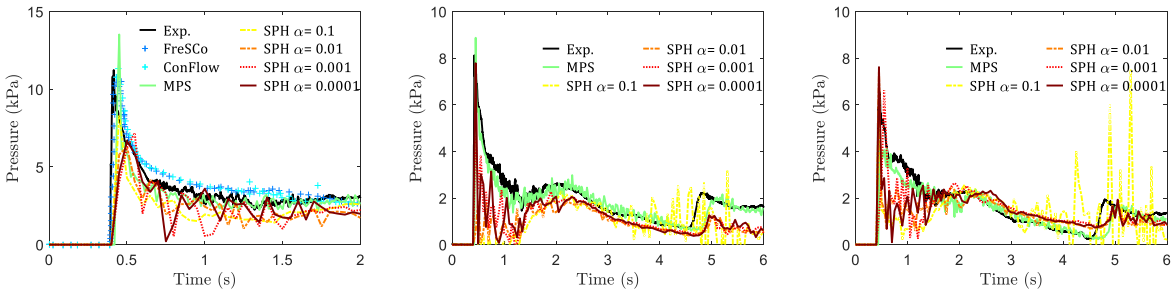

Figure 4. Pressure time series at sensor (a) P_1, (b) P_2 and (c) P_3. Experimental data [14] and numerically computed using FresCo [24], ConFlow [14], MPS and SPH

Table 2. Pressure impulse (I_p) and deviations at sensors P_1, P_2 and P_3. Relative deviations referred to the experiment

Sensor	EXP	SPH								MPS	
		α_0 = 0.1		α_0 = 0.01		α_0 = 0.001		α_0 = 0.0001			
	I_p [Pa.s]	I_p [Pa.s]	[%]	I_p [Pa.s]	[%]	I_p [Pa.s]	[%]	I_p [Pa.s]	[%]	I_p [Pa.s]	[%]
P_1	13392	9519	29.0	9703	27.5	9988	25.4	10217	23.7	12641	5.6
P_2	10961	4898	55.3	5390	50.8	6416	41.5	6506	40.6	10192	7.0
P_3	9500	7189	24.3	7943	16.4	8791	7.5	8736	8.0	8488	10.7

3.2 3D dam-breaking flow – Force

The second case (Case 2) is based on the experiment performed by Aureli et al. [15]. The initial geometry and main dimensions are shown in Fig. 5. The water column, of height $H_w = 0.1$ m, is confined by a gate that is opened with a vertical velocity of 1.25 m/s. Two particle distances, $l_0 = 0.005$ m and 0.0025 m, are used for both methods, and three artificial viscosities are adopted for the SPH. Numerical parameters and processing times are presented in Table 3.

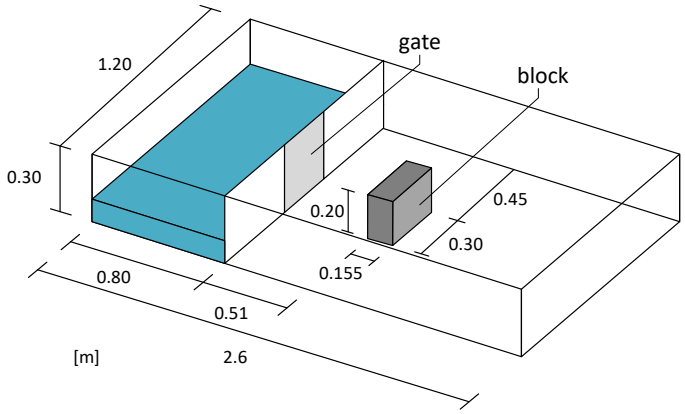

Figure 5. Initial geometry and main dimensions [15]

Table 3. Numerical parameters and processing time of Case 2

Parameter	SPH		MPS	
Viscosity (ν_0)	$1.5\text{x}10^{-3}$, $1.5\text{x}10^{-4}$, $1.5\text{x}10^{-5}$ m²/s	$7.4\text{x}10^{-3}$, $7.4\text{x}10^{-4}$, $7.4\text{x}10^{-5}$ m²/s	10^{-6} m²/s	
Artificial viscosity (α_0)	0.1, 0.01, 0.001		-	
Particle distance (l_0)	0.005 m	0.0025 m	0.005 m	0.0025 m
Radius of support	$2h = 3l_0$		$r_e = 2.1l_0$	
Fluid particles	$7.6\text{x}10^5$	$6.1\text{x}10^6$	$7.7\text{x}10^5$	$6.1\text{x}10^6$
Boundary particles	$2.0\text{x}10^5$	$8.0\text{x}10^5$	$6.7\text{x}10^5$	$2.7\text{x}10^6$
Simulation time	3 s		3 s	
Time step (Δt)	$7\text{x}10^{-5}$ s*	$4\text{x}10^{-5}$ s*	$4\text{x}10^{-4}$ s	$2\text{x}10^{-4}$ s
Computational time	0d0h40m♦	0d9h30m♦	0d5h00m†	6d0h00m†

* Based on the number of computational steps. DualSPHysics uses a variable time steps restrict by CFL and the diffusion stability criteria [13].
♦ GPU Nvidia Tesla K40m, 15 Multiprocessors (2880 cores), clock rate of 0.75 GHz and 11.519 GB of global memory.
† CPU Intel® Xeon® Processor E5 v2 Family, processor base frequency of 2.80 GHz, 20 cores and 126 GB of memory.

Comparisons of the dimensionless velocities fields $|\mathbf{v}|/\sqrt{2gH_w}$ obtained by SPH adopting $\alpha_0 = 0.001$ and MPS, both using the initial particle distance $l_0 = 0.0025$ m, are shown in Fig. 6. Snapshots of the experiment also are presented.

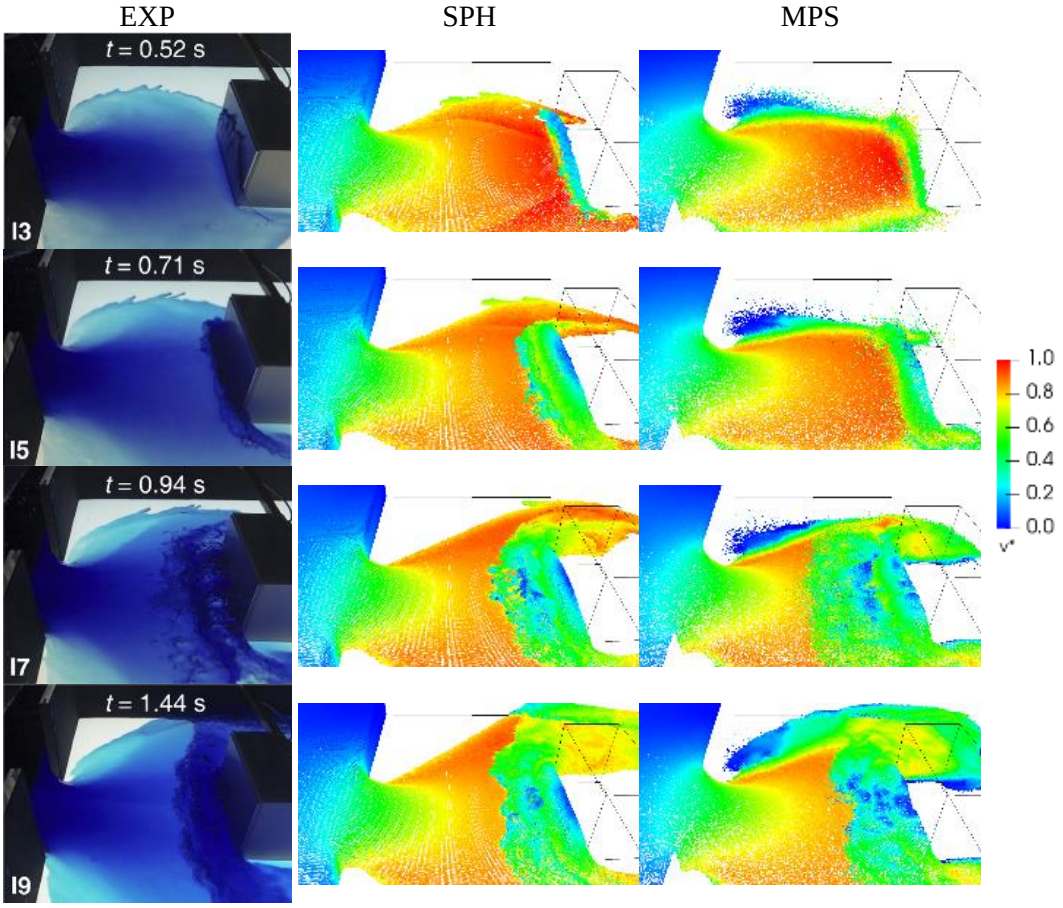

Figure 6. Snapshots of the dam-breaking experiment [15] (left), simulations carried out with SPH adopting $\alpha_0 = 0.001$ (middle) and MPS (right). Particle distance $l_0 = 0.0025$ m

From Fig. 6, the first stages of the wall impact and wave run-up on the wall are well reproduced by both methods. Nevertheless, the flow spreading downstream the gate is better reproduced by the

present MPS simulation. The high-intensity velocity field near the wall computed by the SPH leads to the narrow-spreading flow towards downstream. As pointed out in Aureli et al. [15], SPH is strongly affected by the artificial viscosity, which might be related to the lower flow spreading in the present SPH, even for the lower artificial viscosity cases simulated in the present study.

The experimentally measured average force [15] and the numerically computed forces on the box for $l_0 = 0.005$ m and 0.0025 m are presented in Figs. 7(a) and (b), respectively. It is important to mention how the forces on the box weather side were obtained for each method. For the MPS, the force was calculated by the summation of the pressures of wall particles multiplied by the vertical area of the box. For the SPH, the default output force of DualSPHysics is obtained by the summation of the acceleration of the wall particles, see Eq. (2), multiplied by the mass of the particles at the box weather side. Moreover, accelerations of the wall particles are not considered in the motions of fixed of forced solids in DualSPHysics, i.e., they are used only to obtain the force.

For the simulations with $l_0 = 0.005$ m, illustrated in Fig. 7(a), the numerical wave front propagates more slowly towards the obstacle, and the initial instant of the impact is slightly delayed. The first peak force is underestimated by the MPS, while it is better reproduced by the SPH. After that, forces computed by MPS and SPH, especially when $\alpha_0 = 0.1$, i.e., $\nu_0 = O(10^{-3})$, match well the experimental one.

Higher resolution models with smaller particle distance $l_0 = 0.0025$ m improves the accuracy of the forces computed by MPS and SPH with $\alpha_0 = 0.1$, i.e., $\nu_0 = O(10^{-3})$, as shown in Fig. 7(b). For both simulations, the computed first peak force agrees very well with the experimental one. However, the decrease of the artificial viscosity leads to high-amplitude force oscillations in the SPH.

As in the previous case, see Table 1, the SPH simulations by using GPU reduce significantly the processing time in relation to the MPS simulations by using CPU, see Table 3.

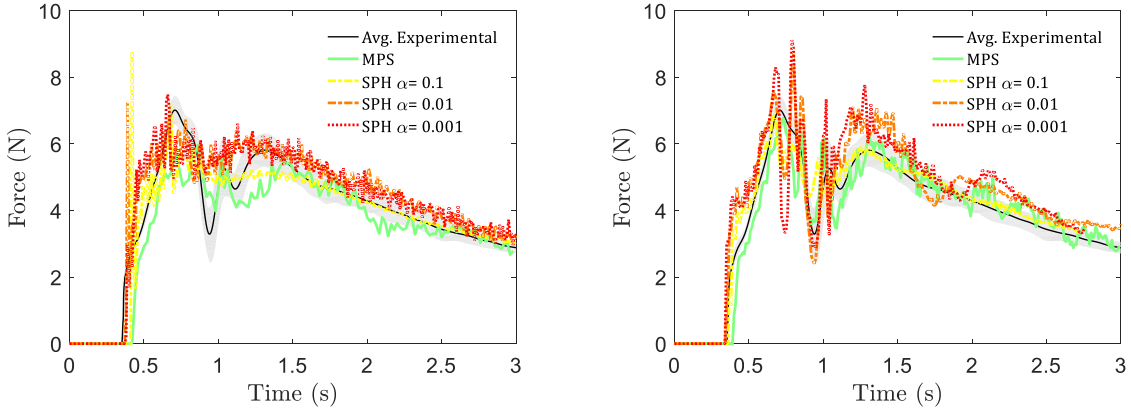

Figure 7. Force time series on the block. Experimentally measured [15] and numerically computed using MPS and SPH for the initial particle distance (a) $l_0 = 0.005$ m and (b) $l_0 = 0.0025$ m

4 Conclusions

In this paper, the comparisons on the accuracy and computational time of the SPH and MPS methods are examined using two 3D dam-breaking cases. Based on the SPH results of the first case, the fluid behavior is well reproduced when $\alpha_0 \leq 0.01$, i.e., $\nu_0 \leq O(10^{-3})$, whereas the pressure impulse deviations indicate that $\alpha_0 \leq 0.001$, i.e., $\nu_0 \leq O(10^{-4})$, is preferable to reproduce the hydrodynamic loads. From the second case, a better approximation of the experimental force is achieved when $\alpha_0 = 0.1$, i.e., $\nu_0 = O(10^{-3})$, while the amplitude force oscillations are larger and increase with the decrease of the artificial viscosity. Therefore, in order to achieve a reasonable result, the artificial viscosity α_0 needs to be tuned for each resolution, providing the equivalent kinematic viscosity ν_0 value in the range of $O(10^{-3})$ to $O(10^{-4})$. Overall, the present MPS reproduced more

accurately the hydrodynamic loads, although both methods provide acceptable results for practical purposes. Furthermore, the adoption of parallel processing in GPU for the SPH significantly reduced the computation time, compared to the conventional serial CPU solver used for MPS. For a better understanding of the relative benefits of the methods for solving free-surface problems, further analysis through practical applications cases are considered by the authors.

Acknowledgements

The first author would like to thank the Coordenação de Aperfeiçoamento de Pessoal de Nível Superior - Brasil (CAPES) - Finance Code 001, for the doctorate scholarship. The first and second authors are also grateful to Petrobras for financial support on the development of the MPS/TPN-USP simulation system based on MPS method.

References

[1] R. A. Gingold and J. J. Monaghan. Smoothed particle hydrodynamics: theory and application to non-spherical stars. *Monthly Notices of the Royal Astronomical Society*, vol. 181, pp. 375-389, 1977.
[2] L. Lucy. A numerical approach to the testing of the fission hypothesis. *Astronomical Journal*, vol. 82, pp. 1013-1024, 1977.
[3] S. Koshizuka and Y. Oka. Moving-particle semi-implicit method for fragmentation of incompressible fluid. *Nuclear Science and Engineering*, vol. 123, n. 3, pp. 421-434, 1996.
[4] H. Gotoh and A. Khayyer. Current achievements and future perspectives for projection-based particle methods with applications in ocean engineering. *Journal of Ocean Engineering and Marine Energy*, vol. 2, n. 3, pp. 251-278, 2016.
[5] D. T. Fernandes, L.-Y. Cheng, E. H. Favero and K. Nishimoto. A domain decomposition strategy for hybrid parallelization of moving particle semi-implicit (MPS) method for computer cluster. *Cluster Computing*, vol. 18, n. 4, pp. 1363-1377, 2015.
[6] C. Hori, H. Gotoh, H. Ikari and A. Khayyer. GPU-acceleration for moving particle semi-implicit method. *Computers & Fluids*, vol. 51, n. 1, pp. 174-183, 2011.
[7] E.-S. Lee, C. Moulinec, R. Xu, D. Violeau, D. Laurence and P. Stansby. Comparisons of weakly compressible and truly incompressible algorithms for the SPH mesh free particle method. *Journal of Computational Physics*, vol. 227, n. 18, pp. 8417-8436, 2008.
[8] S. J. Cummins and M. Rudman. An SPH Projection Method. *Journal of Computational Physics*, vol. 152, n. 2, pp. 584-607, 1999.
[9] J. P. Hughes and D. I. Graham. Comparison of incompressible and weakly-compressible SPH models for free-surface water flows. *Journal of Hydraulic Research*, vol. 48, n. 1, pp. 105-117, 2010.
[10] H. Hashimoto, N. Grenier and D. Le Touzé, 2013. Comparisons of MPS and SPH methods: Forced roll test of a two-dimensional damaged car deck. *Proceedings of Japan Society of Naval Architecture & Ocean Engineering*.
[11] A. M. Abdelrazek, I. Kimura and Y. Shimizu. Comparison between SPH and MPS methods for numerical simulations of free surface flow problems. *Journal of Japan Society of Civil Engineers, Ser. B1 (Hydraulic Engineering)*, vol. 70, n. 4, pp. 67-72, 2014.
[12] F. P. Bakti, M.-H. Kim, K. S. Kim and J.-C. Park. Comparative Study of Standard WC-SPH and MPS Solvers for Free Surface Academic Problems. *International Journal of Offshore and Polar Engineering*, vol. 26, n. 3, pp. 235-243, 2016.
[13] A. J. C. Crespo, J. M. Domínguez, B. D. Rogers, M. Gómez-Gesteira, S. Longshaw, R. Canelas, R. Vacondio, A. Barreiro and O. García-Feal. DualSPHysics: open-source parallel CFD solver on Smoothed Particle Hydrodynamics (SPH). *Computer Physics Communications*, vol. 187, pp. 204-216, 2015.
[14] K. M. T. Kleefsman, G. Fekken, A. E. P. Veldman, I. Iwanowski and B. Buchner. A Volume-of-Fluid based simulation method for wave impact problems. *Journal of Computational Physics*, vol. 76, pp. 363-393, 2005.

[15] F. Aureli, S. Dazzi, A. Maranzoni, P. Mignosa and R. Vacondio. Experimental and numerical evaluation of the force due to the impact of a dam-break wave on a structure. *Advances in Water Resources*, vol. 76, pp. 29-42, 2015.
[16] J. J. Monaghan. Smoothed Particle Hydrodynamics. *Reports on Progress in Physics*, vol. 68, n. 8, pp. 1703-1759, 2005.
[17] J. J. Monaghan. Smoothed Particle Hydrodynamics. *Annual Review of Astronomy and Astrophysics*, vol. 30, pp. 543-574, 1992.
[18] H. Wendland. Piecewise polynomial, positive definite and compactly supported radial functions of minimal degree. *Advances in Computational Mathematics*, vol. 4, n. 1, pp. 389-396, 1995.
[19] D. Molteni and A. Colagrossi. A simple procedure to improve the pressure evaluation in hydrodynamic context using the SPH. *Computer Physics Communications*, vol. 180, n. 6, pp. 861-872, 2009.
[20] J. J. Monaghan. Simulating Free Surface Flows with SPH. *Journal of Computational Physics*, vol. 110, n. 2, pp. 399-406, 1994.
[21] A. J. C. Crespo, M. Gomez-Gesteira and R. A. Dalrymple. Boundary Conditions Generated by Dynamic Particles in SPH Methods. *CMC: Computers, Materials, & Continua*, vol. 5, n. 3, pp. 173-184, 2007.
[22] L. Wang, Q. Jiang and C. Zhang. Improvement of moving particle semi-implicit method for simulation of progressive water waves. *International Journal for Numerical Methods in Fluids*, vol. 85, n. 2, pp. 69-89, 2017.
[23] M. M. Tsukamoto, L.-Y. Cheng and F. K. Motezuki. Fluid interface detection technique based on neighborhood particles centroid deviation (NPCD) for particle methods. *International Journal for Numerical Methods in Fluids*, vol. 82, n. 3, pp. 148-168, 2016.
[24] G. Vaz, F. Jaouen and M. Hoekstra, 2009. Free-Surface Viscous Flow Computations: Validation of URANS Code FreSCo. *Proceedings of J 28th International Conference on Ocean, Offshore and Arctic Engineering*.
[25] O. Flebbe, S. Muenzel, H. Herold, H. Riffert and H. Ruder. Smoothed Particle Hydrodynamics: Physical viscosity and the simulation of accretion disks. *The Astrophysical Journal*, vol. 431, n. 2, pp. 754-760, 1994.
[26] C. Moulinec, R. Issa, J.C. Marongiu and D. Violeau. Parallel 3-D SPH simulations. *Computer Modeling in Engineering and Sciences*, vol. 25, n. 3, pp. 133-148, 2008.